

## CHEMICAL PHYSICS

A spongy nickel-organic CO<sub>2</sub> reduction photocatalyst for nearly 100% selective CO production

Kaiyang Niu,<sup>1,2\*</sup> You Xu,<sup>3,4\*</sup> Haicheng Wang,<sup>2,5\*</sup> Rong Ye,<sup>2,6</sup> Huolin L. Xin,<sup>7</sup> Feng Lin,<sup>8</sup> Chixia Tian,<sup>9</sup> Yanwei Lum,<sup>1,2</sup> Karen C. Bustillo,<sup>10</sup> Marca M. Doeff,<sup>9</sup> Marc T. M. Koper,<sup>11</sup> Joel Ager,<sup>1,2</sup> Rong Xu,<sup>3,4†</sup> Haimei Zheng<sup>1,2†</sup>

Solar-driven photocatalytic conversion of CO<sub>2</sub> into fuels has attracted a lot of interest; however, developing active catalysts that can selectively convert CO<sub>2</sub> to fuels with desirable reaction products remains a grand challenge. For instance, complete suppression of the competing H<sub>2</sub> evolution during photocatalytic CO<sub>2</sub>-to-CO conversion has not been achieved before. We design and synthesize a spongy nickel-organic heterogeneous photocatalyst via a photochemical route. The catalyst has a crystalline network architecture with a high concentration of defects. It is highly active in converting CO<sub>2</sub> to CO, with a production rate of  $\sim 1.6 \times 10^4 \mu\text{mol hour}^{-1} \text{g}^{-1}$ . No measurable H<sub>2</sub> is generated during the reaction, leading to nearly 100% selective CO production over H<sub>2</sub> evolution. When the spongy Ni-organic catalyst is enriched with Rh or Ag nanocrystals, the controlled photocatalytic CO<sub>2</sub> reduction reactions generate formic acid and acetic acid. Achieving such a spongy nickel-organic photocatalyst is a critical step toward practical production of high-value multicarbon fuels using solar energy.

## INTRODUCTION

Rapid fossil fuel consumption induces environmental burden and energy crisis (1–3). Excessive anthropogenic CO<sub>2</sub> emission is a significant concern because of its hastening impact on climate change (4–6), acidification of ocean (7), crop yield reduction (8), extinction of animal species (9), and damage to human health (10, 11). Removal of excessive CO<sub>2</sub> from the atmosphere (12), particularly converting CO<sub>2</sub> to fuels using solar energy, is currently a global research endeavor (13–15). Discovering novel catalysts that can reduce the stable CO<sub>2</sub> molecules and convert them to liquid fuels with high activity and selectivity is essential (13, 14). To date, despite the progress that has been made in investigating the photocatalytic reduction of CO<sub>2</sub> (15–19), controlling the reaction to yield a specific product among many possible reaction species, including CO, H<sub>2</sub>, CH<sub>4</sub>, and formic acid, remains a great challenge (16, 20, 21). Finding photocatalysts that can efficiently convert CO<sub>2</sub> to CO and largely suppress other competing photocatalytic reactions, such as H<sub>2</sub> evolution, would be a critical step forward toward practical solar-to-fuels conversion for the production of high-value multicarbon fuels (15, 17, 22).

We recently developed a laser-chemical method and synthesized active transition metal hydroxide catalysts with a high concentration of defects for water oxidation (23). Specifically, we used an unfocused infrared laser to initiate the reactions between transition metal ions and triethylene glycol (TEG) and obtained a series of metal hydroxide-TEG

composites with a distorted layered structure (23). This disordered structure enhances the accessibility of water molecules to the active sites and enables efficient electrocatalysis of alkaline water oxidation (23). Such a laser-chemical strategy may be applied to the discovery of many other catalysts, for instance, novel nanostructured metal-organic heterogeneous catalysts for CO<sub>2</sub> reduction reaction.

When designing catalysts for CO<sub>2</sub> reduction, the material's ability to capture the CO<sub>2</sub> molecules is another significant consideration (24). Metal-organic frameworks (MOFs) with high surface area and tunable pores have been used for gas capture and heterogeneous catalysis (25, 26). Typically, MOFs have highly ordered crystalline structures constructed by coordinating metal ions or clusters with rigid organic linkers, most often the aromatic carboxylic acid molecules (27), such as terephthalic acid (TPA). In light of MOF structure design, we replace part of the rigid linkers (for example, TPA) in traditional MOFs with soft molecules (for example, TEG) by laser, considering the comparable molecular length of TEG to TPA (fig. S1). When the TEG molecules, which lack essential carboxylic groups for the perfect framework construction, are weaved into the metal-TPA framework, their substitution of TPA linkers may frustrate the growth of highly ordered MOF crystals, resulting in disordered and defective metal-organic hybrids for effective CO<sub>2</sub> fixation.

Here, we design a model metal-organic CO<sub>2</sub> reduction catalyst, with Ni<sup>2+</sup> ions as active metal centers, TPA as a rigid linker, TEG as a soft linker, and dimethylformamide (DMF) as a solvent, via laser-induced solution reactions. The as-synthesized catalyst, labeled as Ni(TPA/TEG), has a crystalline network architecture with considerable defects and performs nearly 100% selective gas production (CO over H<sub>2</sub> evolution) with a high CO production rate of  $\sim 1.6 \times 10^4 \mu\text{mol hour}^{-1} \text{g}^{-1}$ . Further metal decorations (that is, Rh and Ag) of the Ni(TPA/TEG) catalyst lead to controlled photocatalytic CO<sub>2</sub> reduction reactions that generate formic acid and acetic acid.

## RESULTS AND DISCUSSION

## Structure determination of the Ni(TPA/TEG) catalyst

As shown in Fig. 1A, the Ni(TPA/TEG) composite forms a disordered spongy network structure, in which Ni, O, and C are uniformly distributed (fig. S2). In comparison, the solution without TEG, Ni(TPA) only,

<sup>1</sup>Department of Materials Science and Engineering, University of California, Berkeley, Berkeley, CA 94720, USA. <sup>2</sup>Materials Sciences Division, Lawrence Berkeley National Laboratory, Berkeley, CA 94720, USA. <sup>3</sup>School of Chemical and Biomedical Engineering, Nanyang Technological University, 62 Nanyang Drive, Singapore 637459, Singapore. <sup>4</sup>SinBeRISE (Singapore-Berkeley Research Initiative for Sustainable Energy) CREATE, 1 Create Way, Singapore 138602, Singapore. <sup>5</sup>National Center for Materials Service Safety, University of Science and Technology Beijing, Beijing 100083, P. R. China. <sup>6</sup>Department of Chemistry, University of California, Berkeley, Berkeley, CA 94720, USA. <sup>7</sup>Center for Functional Nanomaterials, Brookhaven National Laboratory, Upton, NY 11973, USA. <sup>8</sup>Department of Chemistry, Virginia Tech, Blacksburg, VA 24061, USA. <sup>9</sup>Energy Storage and Distributed Resources Division, Lawrence Berkeley National Laboratory, Berkeley, CA 94720, USA. <sup>10</sup>National Center for Electron Microscopy, Molecular Foundry, Lawrence Berkeley National Laboratory, Berkeley, CA 94720, USA. <sup>11</sup>Leiden Institute of Chemistry, Leiden University, 2300 RA Leiden, Netherlands. \*These authors contributed equally to this work.

†Corresponding author. Email: rxu@ntu.edu.sg (R.X.); hmzheng@lbl.gov (H.Z.)

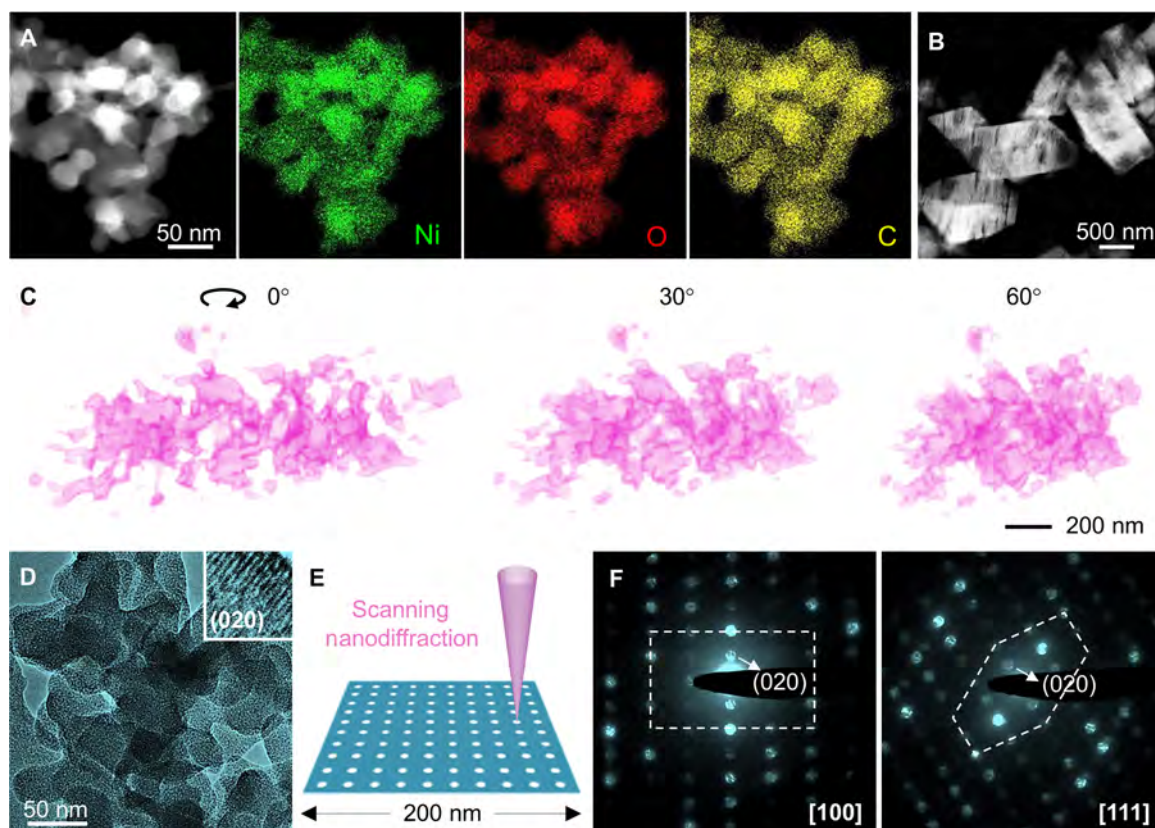


**Fig. 1. Structure of the laser-chemical tailored spongy Ni(TPA/TEG) catalyst.** (A) Scanning TEM (STEM) images and energy-dispersive x-ray spectroscopy (EDX) mapping of the spongy Ni(TPA/TEG) nanostructure. (B) STEM image of the Ni(TPA/TEG) particles. (C) Three-dimensional tomographic reconstruction of a fraction of spongy Ni(TPA/TEG) composite (movie S1). (D) TEM image of the spongy Ni(TPA/TEG) nanostructure. The inset high-resolution TEM image displays the defective (020) lattices [ $d_{(020)} = 1.02$  nm] of an orthorhombic crystal. (E) Scanning electron nanodiffraction series taken from the Ni(TPA/TEG) particle by a scanning nanoprobe with an electron beam size of  $\sim 3$  nm. The probe step size is 10 nm with an exposure time of 0.5 s at each step and a total beam current of  $\sim 5$  pA. (F) Diffraction patterns showing the [100] and [111] orientations of the orthorhombic Ni(TPA/TEG) composite (movies S2 and S3). The dimensions of the diffraction patterns are  $11.9 \text{ nm}^{-1} \times 11.9 \text{ nm}^{-1}$ .

forms large particles (Fig. 1B). A three-dimensional electron tomographic reconstruction of the spongy Ni(TPA/TEG) architecture reveals various mesopores in the structure (Fig. 1C and movie S1), which closely resembles the pore features identified from the  $\text{N}_2$  physisorption measurements (fig. S3). Figure 1D shows a typical transmission electron microscopy (TEM) image of the spongy Ni(TPA/TEG) composite, where defective lattices with a  $d$ -spacing of 1.02 nm are captured. To further interpret the structure of Ni(TPA/TEG) composite, we acquire a scanning nanobeam diffraction data set using an electron beam with a size of  $\sim 3$  nm, a total beam current of  $\sim 5$  pA, and an exposure time of 0.5 s, where the electron beam damage to the metal-organic material has been evidently minimized (Fig. 1E). Single-crystalline diffraction patterns along the [100] and [111] orientations of the Ni(TPA/TEG) composite are captured from two different regions of the spongy network (Fig. 1F and movies S2 and S3), showing an orthorhombic structure similar to that of the Ni(TPA) particles (fig. S4). Changes of the diffraction patterns are observed from movies S2 and S3, indicating defects (that is, grain boundaries) in the spongy Ni(TPA/TEG) catalyst (fig. S5).

To verify that the soft TEG molecules have been incorporated into the Ni(TPA) framework (Fig. 2A), we compare the structure of laser-synthesized Ni(TPA) and Ni(TPA/TEG) composites in detail. The x-ray diffraction (XRD) pattern (Fig. 2B) shows that the Ni(TPA) composite has an orthorhombic structure where the Ni-TPA units construct the

framework (fig. S4). The spongy Ni(TPA/TEG) has a crystal structure similar to that of Ni(TPA), but slight differences exist in the peak positions and widths of the x-ray lines, which may result from the exchange of linkers and solvent molecules in the structure (28). In the Fourier transform infrared (FTIR) spectra (Fig. 2C), we can see that both samples have clear bands of  $\nu(\text{COO}^-)$  ( $1375$  and  $1575 \text{ cm}^{-1}$ ) and ring breathing ( $815 \text{ cm}^{-1}$ ) from the TPA linkers. Characteristic bands of  $\delta\text{NCO}$  ( $690 \text{ cm}^{-1}$ ) and  $\nu(\text{CO})$  ( $1685 \text{ cm}^{-1}$ ) from DMF molecules are found in Ni(TPA), indicating that DMF molecules may reside in the MOF cavities and coordinate with  $\text{Ni}^{2+}$  through carbonyl groups (28). Meanwhile, distinct bands of  $\nu(\text{OH})$  ( $1065$  and  $3374 \text{ cm}^{-1}$ ) related to TEG are found exclusively in Ni(TPA/TEG), and no DMF bands are detected, indicating that TEG molecules exist in Ni(TPA/TEG); DMF molecules that originally occupied the Ni(TPA) framework cavities prefer to leave. The EDX spectrum (Fig. 2D) also shows that no nitrogen (from DMF) can be detected in Ni(TPA/TEG). Thermogravimetric analysis (TGA) curves in Fig. 2E, both displaying three stages of mass losses, indicate differences between the two samples. For Ni(TPA), the mass loss measurements of 6, 18, and 50% are from  $\text{H}_2\text{O}$ , DMF, and TPA, respectively (28); for Ni(TPA/TEG), the mass losses of 16, 26, and 26% are from  $\text{H}_2\text{O}$ , TEG, and TPA, respectively. The large differences in the mass loss of TPA in the two samples (50% versus 26%) indicate that soft TEG molecules have replaced part of the rigid TPA linkers, causing the formation of a spongy Ni(TPA/TEG)

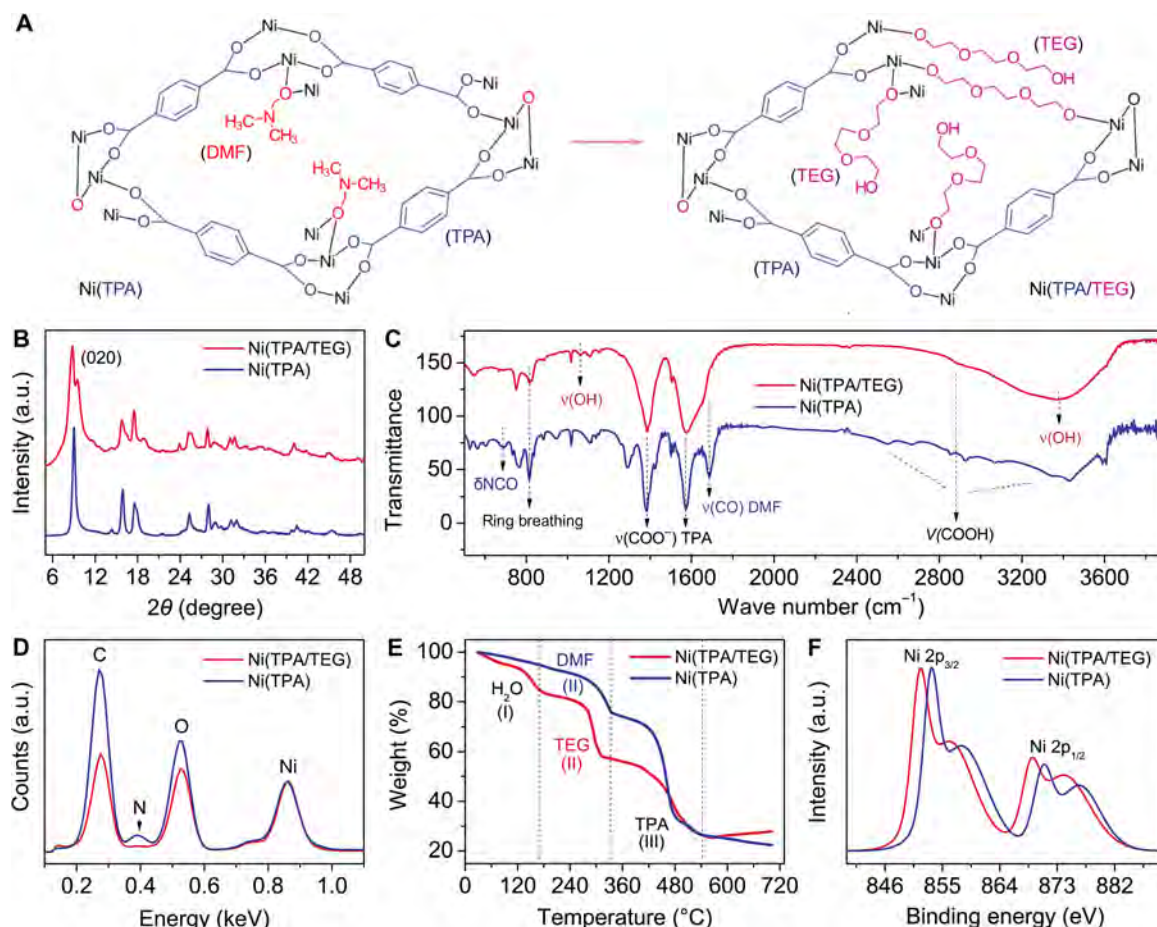


**Fig. 2. Comparison of laser-chemical tailored Ni(TPA/TEG) and Ni(TPA) composites.** (A) Proposed design strategy of the disordered spongy Ni(TPA/TEG) composite by introducing soft Ni-TEG building units into a Ni(TPA) framework through laser-chemical reaction. XRD patterns (B), FTIR spectra (C), EDX spectra (D), TGA curves (E), and XPS spectra (F) of the laser-chemical tailored Ni(TPA/TEG) and Ni(TPA) composites. a.u., arbitrary units.

network. Because of the varying chemical environment of  $\text{Ni}^{2+}$ , the Ni $2p$  peaks in the x-ray photoelectron spectroscopy (XPS) spectra (Fig. 2F) shifted to the right in Ni(TPA/TEG) compared to Ni(TPA).

We also find that it is more effective to use lasers to cross-link the soft TEG and rigid TPA molecules together with the  $\text{Ni}^{2+}$  centers than to use a traditional heating process (see the Supplementary Materials). Laser irradiation appears to produce Ni-TEG building units that are indispensable for the spongy Ni(TPA/TEG) network construction (Fig. 2A). Because of the soft character of TEG molecules, various inhomogeneous configurations of Ni-TEG units can be generated. Mismatches between the soft Ni-TEG units and the rigid Ni-TPA units may introduce considerable defects, leading to the formation of disordered spongy Ni(TPA/TEG).

### Evaluation of the photocatalytic activity for CO production

We apply the as-synthesized Ni-organic composites for visible light-driven photocatalytic  $\text{CO}_2$  reduction in a solvent mixture of acetonitrile/water [considering the high solubility of  $\text{CO}_2$  in acetonitrile (29)] under mild reaction conditions (20°C and 400 torr of  $\text{CO}_2$ ), with triethanolamine (TEOA) as a sacrificial reducing agent and  $\text{Ru}(\text{bpy})_3\text{Cl}_2 \cdot \text{H}_2\text{O}$  as a photosensitizer (18, 30). Five samples (figs. S6 to S8), that is, Ni(TPA) (L), Ni(TPA) (H), Ni(TPA/TEG) (L), Ni(TPA/TEG) (H), and Ni(TEG) (L), synthesized by both laser irra-

diation (L) and traditional heating (H), are examined. Figure 3A shows the CO evolutions from these five Ni-organic catalysts in a 6-hour photocatalytic reaction. The spongy Ni(TPA/TEG) (L) composite shows the highest activity, and the amount of CO is 95.2  $\mu\text{mol}$  after a 2-hour reaction, giving a CO production rate of 15,866  $\mu\text{mol hour}^{-1} \text{g}^{-1}$ , which is several times higher than that from other samples. The total amount of CO produced on the spongy Ni(TPA/TEG) catalyst in 6 hours reaches 136.9  $\mu\text{mol}$  (Fig. 3A), giving a turnover number of 11.5 for the 6-hour reaction (table S1). The CO production rate is also superior compared with many other reported heterogeneous CO evolution photocatalysts to the best our knowledge (17), such as the  $\text{Co}_3\text{O}_4$  platelets with  $[\text{Ru}(\text{bpy})_3]\text{Cl}_2$  as a photosensitizer (3523  $\mu\text{mol hour}^{-1} \text{g}^{-1}$ ) (18), the sensitized  $\text{TiO}_2$  particles with enzyme as a cocatalyst (300  $\mu\text{mol hour}^{-1} \text{g}^{-1}$ ) (31), and the sensitized  $\text{BaLa}_4\text{Ti}_4\text{O}_{15}$  particles with Ag as a cocatalyst (22  $\mu\text{mol hour}^{-1} \text{g}^{-1}$ ) (16). Note that the soluble homogeneous metal complex catalysts, which have also been investigated for controlled  $\text{CO}_2$  reduction (32–34), are not categorized here for comparison.

By testing the 2-hour yield of CO on different amounts of the Ni(TPA/TEG) catalyst, we obtain a roughly linear relationship between the amount of evolved CO and the amount of the catalyst (Fig. 3B). However, kinetically, we found that the CO production rate actually decreases with the increase in the amount of the catalyst

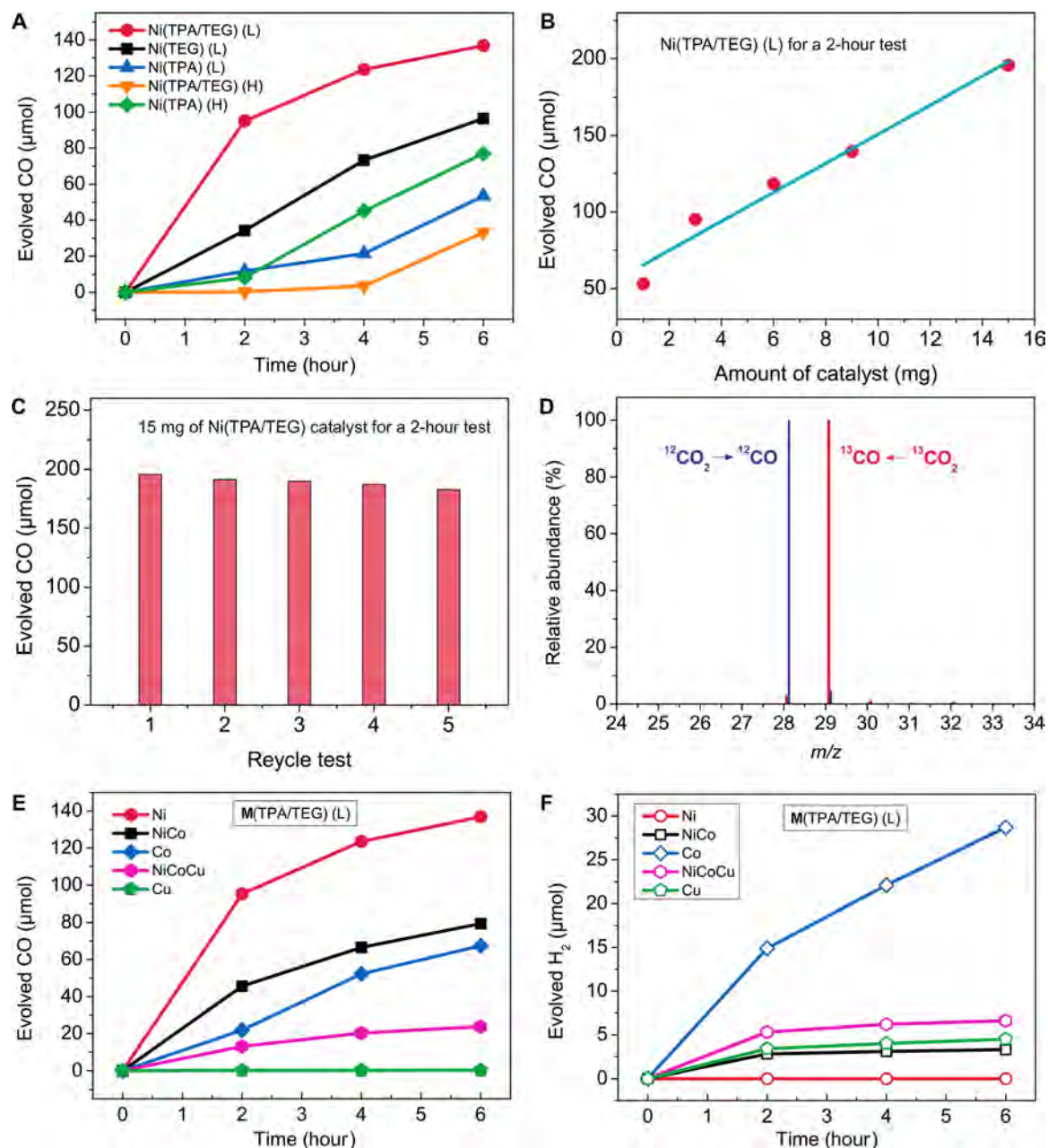


**Fig. 3. Conversion of CO<sub>2</sub> to CO by photocatalysis.** (A) CO evolution on five Ni-based catalysts with different combinations of TPA, TEG, and DMF. The composites synthesized by laser-chemical approach are labeled with “L”; the ones synthesized by traditional heating method are marked with “H.” (B) CO production on different amounts of the Ni(TPA/TEG) catalyst. (C) Average yield of CO in the first 2 hours for five recycling tests. (D) MS of <sup>12</sup>CO (blue lines) and <sup>13</sup>CO (red lines) produced on the spongy Ni(TPA/TEG) catalyst by using <sup>12</sup>CO<sub>2</sub> and <sup>13</sup>CO<sub>2</sub> as gas sources, respectively. *m/z*, mass/charge ratio. (E) Comparison of CO evolution on five laser-synthesized *M*(TPA/TEG) (*M* = Ni, Co, Cu) catalysts. (F) Comparison of H<sub>2</sub> evolution on the five *M*(TPA/TEG) catalysts.

(fig. S9), where 1.0 mg of the Ni(TPA/TEG) catalyst gives a CO production rate of  $\sim 26,620 \mu\text{mol hour}^{-1} \text{g}^{-1}$  in the same solution, indicating that more electrons generated from the photosensitizer molecules could have been transferred to the catalytic active sites. We have also tested the reusability of the spongy Ni(TPA/TEG) catalyst upon each 2-hour photocatalysis, where the catalyst has kept its activity and selectivity after recycling (Fig. 3C). It also exhibits excellent structural stability, and no obvious structural change is found after 24 hours of photocatalysis (fig. S10). To confirm the origin of the as-produced CO, we use isotopic <sup>13</sup>CO<sub>2</sub> as feedstock gas for the photocatalytic re-

duction and examine the products by gas chromatography–mass spectrometry (GC-MS). A major signal at a mass/charge ratio of 29 on the mass spectrum corresponding to <sup>13</sup>CO (Fig. 3D, red lines) appears, which confirms that the as-detected CO originates from the CO<sub>2</sub> gas source (fig. S11).

Transition metal ions with switchable electronic states have long been considered promising active sites for diverse photocatalytic or electrocatalytic reactions, such as water splitting (35–37), CO oxidation (38), and CO<sub>2</sub> reduction (39). Consequently, we use the laser-chemical method to synthesize four additional samples and compare different

metal ions, that is,  $\text{Ni}^{2+}$ ,  $\text{Co}^{2+}$ , and  $\text{Cu}^{2+}$  (fig. S12), as active sites for the photocatalytic  $\text{CO}_2$  reduction. Results show that the spongy  $\text{Ni}(\text{TPA}/\text{TEG})$  catalyst is still the most active catalyst for CO evolution, and the activity worsens with the incorporation of Co and Cu ions (Fig. 3E). The amount of CO generated on the  $\text{Ni}(\text{TPA}/\text{TEG})$  catalyst is almost two times that of the CO generated from  $\text{Co}(\text{TPA}/\text{TEG})$  in a 6-hour photocatalytic reaction. The  $\text{Cu}(\text{TPA}/\text{TEG})$  catalyst barely generates any CO, which is distinctly different from the metal Cu catalyst that has superior activity for CO evolution from the electrocatalytic reduction of  $\text{CO}_2$  (40).

### Evaluation of the CO production selectivity

We find that CO ( $\text{CO}_2 + \text{H}_2\text{O} + 2e^- \rightarrow \text{CO} + 2\text{OH}^-$ ) is the only detectable gas product from the photocatalytic  $\text{CO}_2$  reduction on the TPA-containing Ni-organic catalysts.  $\text{H}_2$  evolution ( $2\text{H}_2\text{O} + 2e^- \rightarrow \text{H}_2 + 2\text{OH}^-$ ), usually acting as a major competing reaction in the  $\text{CO}_2$  reduction system for many transition metal-based catalysts (18, 20), has been completely suppressed (table S1). Thus, a near 100% selectivity of CO production (over  $\text{H}_2$  evolution) is achieved. Note that no other potential competing gas products, such as  $\text{CH}_4$  and  $\text{C}_2\text{H}_4$  (17), have been detected in our experiments either.

For comparison, we have detected considerable amounts of  $\text{H}_2$  from other laser-synthesized  $M(\text{TPA}/\text{TEG})$  ( $M = \text{Ni}, \text{Co}, \text{Cu}$ ) catalysts (Fig. 3, E and F, and fig. S13), and CO selectivity values of 96, 70, 78.2, and 4.8% were measured for  $\text{NiCo}(\text{TPA}/\text{TEG})$ ,  $\text{Co}(\text{TPA}/\text{TEG})$ ,  $\text{NiCoCu}(\text{TPA}/\text{TEG})$ , and  $\text{Cu}(\text{TPA}/\text{TEG})$ , respectively. We have also detected a fair

amount of  $\text{H}_2$  (25.7  $\mu\text{mol}$ ) from the hydroxylated TPA-free  $\text{Ni}(\text{TEG})$  catalyst in addition to the CO evolution (96.5  $\mu\text{mol}$ ) after a 6-hour reaction (fig. S14), which is analogous to the Ni-based hydroxides for practical  $\text{H}_2$  evolution from the electrocatalysis of water (36).

### Tuning the selectivity for liquid fuels production from $\text{CO}_2$

Furthermore, considering the potential of noble metal electrodes for  $\text{CO}_2$  reduction (41, 42), we decorate the spongy  $\text{Ni}(\text{TPA}/\text{TEG})$  with noble metal nanocrystals, that is, Rh and Ag, in pursuit of tuning the selectivity of liquid fuels production from the photocatalytic  $\text{CO}_2$  reduction (15, 21). Figure 4 (A to C) shows the Ag-decorated  $\text{Ni}(\text{TPA}/\text{TEG})$  catalyst, where Ag nanocrystals with an average diameter of  $\sim 6$  nm are well dispersed on the  $\text{Ni}(\text{TPA}/\text{TEG})$ . We examine the liquid products after a 6-hour reaction on three catalysts, that is, undecorated  $\text{Ni}(\text{TPA}/\text{TEG})$ , Rh-decorated  $\text{Ni}(\text{TPA}/\text{TEG})$ , and Ag-decorated  $\text{Ni}(\text{TPA}/\text{TEG})$  (Fig. 4D). For the  $\text{Ni}(\text{TPA}/\text{TEG})$  catalyst without any decoration, we measure formic acid (HCOOH) with a concentration of 29.2  $\mu\text{M}$  and acetic acid ( $\text{CH}_3\text{COOH}$ ) with a concentration of 72.5  $\mu\text{M}$  in addition to CO. With the decoration of Rh and Ag nanocrystals, the amounts of CO decrease drastically, whereas the amounts of liquid products significantly increase. Formic acid (HCOOH) with a concentration of 313.5  $\mu\text{M}$  is mainly obtained on the Rh-decorated  $\text{Ni}(\text{TPA}/\text{TEG})$  catalyst, and  $\text{CH}_3\text{COOH}$  with a concentration of 195.6  $\mu\text{M}$  is the major product for the Ag-decorated  $\text{Ni}(\text{TPA}/\text{TEG})$  catalyst, where the origin of  $\text{CH}_3\text{COOH}$  has been confirmed from the flowing  $\text{CO}_2$  source by MS (fig. S15). Note that CO,

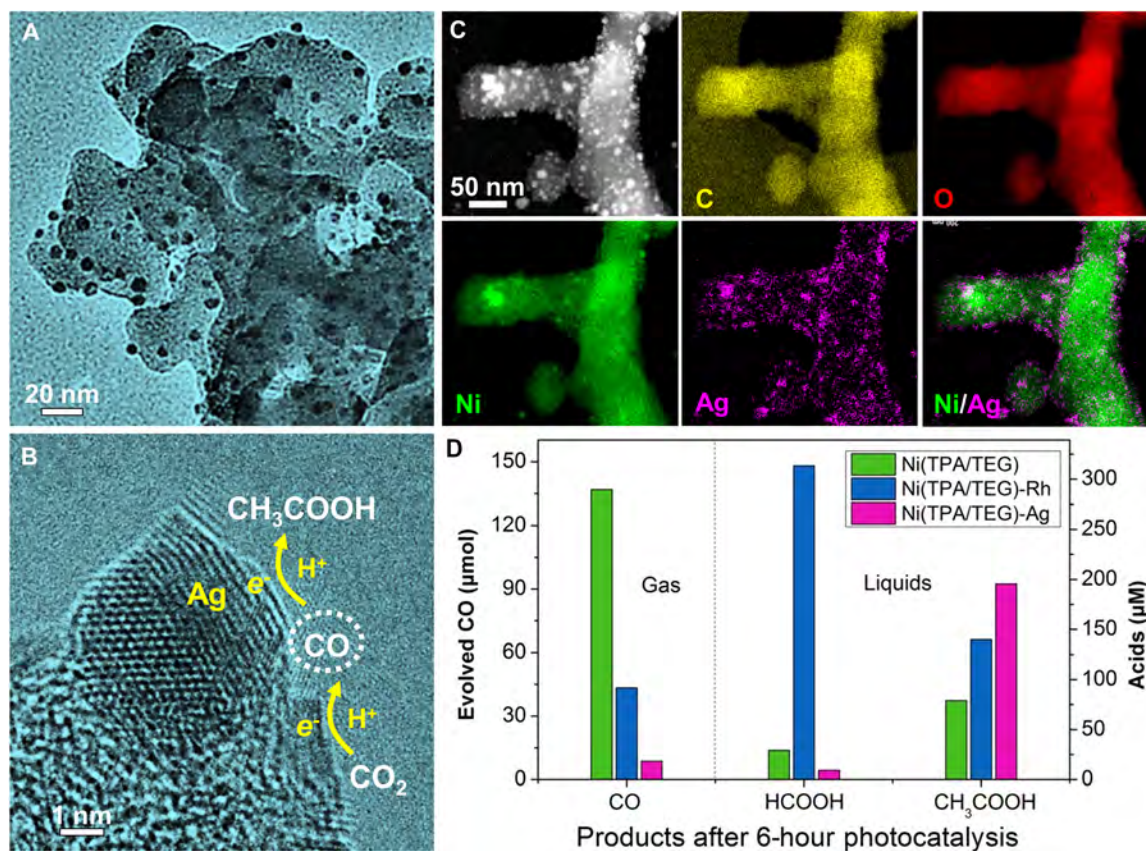


**Fig. 4. Generation of liquid products on metal-decorated  $\text{Ni}(\text{TPA}/\text{TEG})$  composites.** Low-magnification (A) and high-resolution (B) TEM images of the  $\text{Ni}(\text{TPA}/\text{TEG})$  composite decorated with Ag nanocrystals. (C) EDX mapping of the as-prepared  $\text{Ni}(\text{TPA}/\text{TEG})$ -Ag composite. (D) Comparison of the amount of the products (CO, HCOOH, and  $\text{CH}_3\text{COOH}$ ) generated from photocatalytic  $\text{CO}_2$  reduction on  $\text{Ni}(\text{TPA}/\text{TEG})$ ,  $\text{Ni}(\text{TPA}/\text{TEG})$ -Rh, and  $\text{Ni}(\text{TPA}/\text{TEG})$ -Ag catalysts.

formic acid, and acetic acid reflect the overall product distribution of the photocatalytic CO<sub>2</sub> reduction reaction; no other liquid products, such as methanol, ethanol, or propanol, are detected in this experiment.

### Enhanced production of liquid fuels from photocatalytic reduction of CO

By assuming that the evolved CO may be further consumed for the production of acids, we also conduct control experiments using CO, instead of CO<sub>2</sub>, as the gas feedstock for the photocatalytic reduction reaction. As a result, largely enhanced yields of acids are obtained. For instance, the amount of HCOOH evolved from the CO reduction is 24 times higher than that from the CO<sub>2</sub> reduction on the Ni(NPA/TEG) catalyst (Fig. 5A), and the amount of CH<sub>3</sub>COOH produced from the CO reduction reaction for the Ag/Rh-decorated Ni(NPA/TEG) catalyst exhibits a sixfold increase over the results from the CO<sub>2</sub> reduction reaction (Fig. 5B and fig. S16). Besides the increase in acid production, another important C2 product, that is, ethanol [with a concentration of 270.6 μM for Ni(NPA/TEG)-Rh and 262.2 μM for Ni(NPA/TEG)-Ag], has also emerged from the 6-hour photocatalytic CO reduction reaction.

### Possible mechanisms for the photocatalytic reduction reactions of CO<sub>2</sub> or CO

On the basis of the abovementioned results, we propose the following mechanism for the photocatalytic CO<sub>2</sub> reduction reactions on the

spongy Ni(TPA/TEG) catalyst (Fig. 6). Upon visible light irradiation, the photosensitizer [Ru(bpy)<sub>3</sub>]<sup>2+</sup> is excited and then reductively quenched by the TEOA sacrificial electron donor (18, 30, 43), which gives rise to the reduced species of [Ru(bpy)<sub>3</sub>]<sup>2+</sup> (Fig. 6A). Subsequently, the reduced species of [Ru(bpy)<sub>3</sub>]<sup>2+</sup> could transfer an electron to the spongy Ni(TPA/TEG) catalyst, which then participates in reducing the CO<sub>2</sub> molecules fixed on the catalyst (Fig. 6B). In the 2-hour yield tests of CO production in the solution with different amounts of Ni(TPA/TEG), we have found that the CO production rate decreases with the increase in the amount of catalyst (fig. S9), indicating that the electron transfer from [Ru(bpy)<sub>3</sub>]<sup>2+</sup> to the catalyst could be a rate-determining step for the CO<sub>2</sub> reduction reaction, where a diffusion-limited event may have occurred in this heterogeneous catalytic system (44).

For the selective generation of CO from CO<sub>2</sub>, we propose the formation of a basic intermediate (45) [that is, CO<sub>2</sub> radical anion (CO<sub>2</sub><sup>•-</sup>)] in the initial reaction step (CO<sub>2</sub> + e<sup>-</sup> → CO<sub>2</sub><sup>•-</sup>), which acts as a Brønsted base and reacts easily with H<sub>2</sub>O to form CO (CO<sub>2</sub><sup>•-</sup> + H<sub>2</sub>O + e<sup>-</sup> → CO + 2OH<sup>-</sup>). On the other hand, in our proton-deficient photocatalytic reaction medium (pH 8), water (the proton donor) could provide another nonbasic intermediate, H<sup>•</sup> (H<sub>2</sub>O + e<sup>-</sup> → H<sup>•</sup> + OH<sup>-</sup>), before the H<sub>2</sub> evolution (H<sub>2</sub>O + H<sup>•</sup> + e<sup>-</sup> → H<sub>2</sub> + OH<sup>-</sup>) (46). For the spongy Ni(TPA/TEG) catalyst, it is likely that the Ni-TPA coordination units are unfavorable for the binding of H<sup>•</sup> on the active sites, limiting the proton transfer and the formation of H<sub>2</sub>. In addition, the flexible Ni-TEG units, with superior structural resistance to the aqueous environment (23), enable the disordered spongy network construction, where the open and defective structure provides more accessible Ni<sup>2+</sup> active sites to capture and stabilize the CO<sub>2</sub><sup>•-</sup> intermediates, leading to the efficient production of CO.

Subsequently, the evolved CO can be further reduced to liquid fuels through proton-coupled multielectron reaction processes (Fig. 6C and fig. S17). Figure 6D shows the proposed conversion pathways leading to the formation of HCOOH, CH<sub>3</sub>COOH, and CH<sub>3</sub>CH<sub>2</sub>OH via proton-coupled one-, four-, and eight-electron steps, respectively, in the electrolyte with a pH value of ~8. For the formation of HCOOH, we propose the following reactions



where \*CO is quickly protonated to \*CHO and then hydroxylated to HCOOH. In the pathway of CH<sub>3</sub>COOH formation, \*CO is continuously hydrated to \*CHO → \*CHOH → \*CH<sub>2</sub>OH → \*CH<sub>3</sub>OH, which bonds with the adsorbed \*CO to form CH<sub>3</sub>COOH. As to the formation of CH<sub>3</sub>CH<sub>2</sub>OH, the dehydroxylation of the as-formed \*CHO could be a critical rate-limiting step to produce \*C that can be further protonated to \*CH → \*CH<sub>2</sub> → \*CH<sub>3</sub> (47), and the C-C coupling between \*CH<sub>3</sub> and multiprotonated \*CO (that is, CH<sub>2</sub>OH) could lead to the formation of CH<sub>3</sub>CH<sub>2</sub>OH (48).

To further tune the proposed reactions, we performed the CO reduction reaction on the Ni(TPA/TEG)-Ag in the electrolyte with a pH value of ~13 (fig. S18). We found that CH<sub>3</sub>OH (184.09 μM), CH<sub>3</sub>CH<sub>2</sub>OH (149.39 μM), HCOOH (438.98 μM), and CH<sub>3</sub>COOH (276.99 μM) are produced at pH 13 in 6 hours, which is distinct from the liquid products generated at pH 8, that is, CH<sub>3</sub>OH (0 μM), CH<sub>3</sub>CH<sub>2</sub>OH

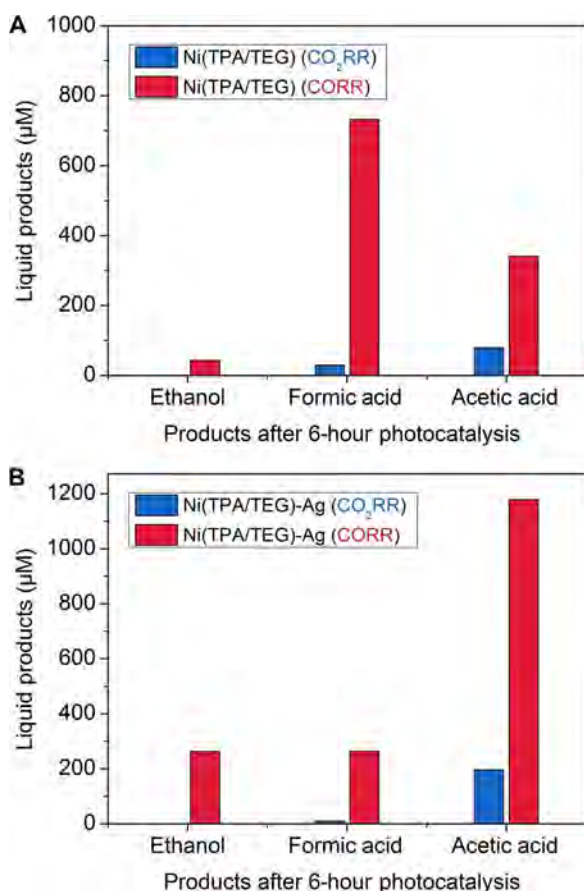


**Fig. 5. Comparison of the liquid products generated from photocatalytic CO<sub>2</sub> reduction reactions (CO<sub>2</sub>RR) and CO reduction reactions (CORR) on two catalysts. (A) Ni(TPA/TEG). (B) Ni(TPA/TEG)-Ag.**

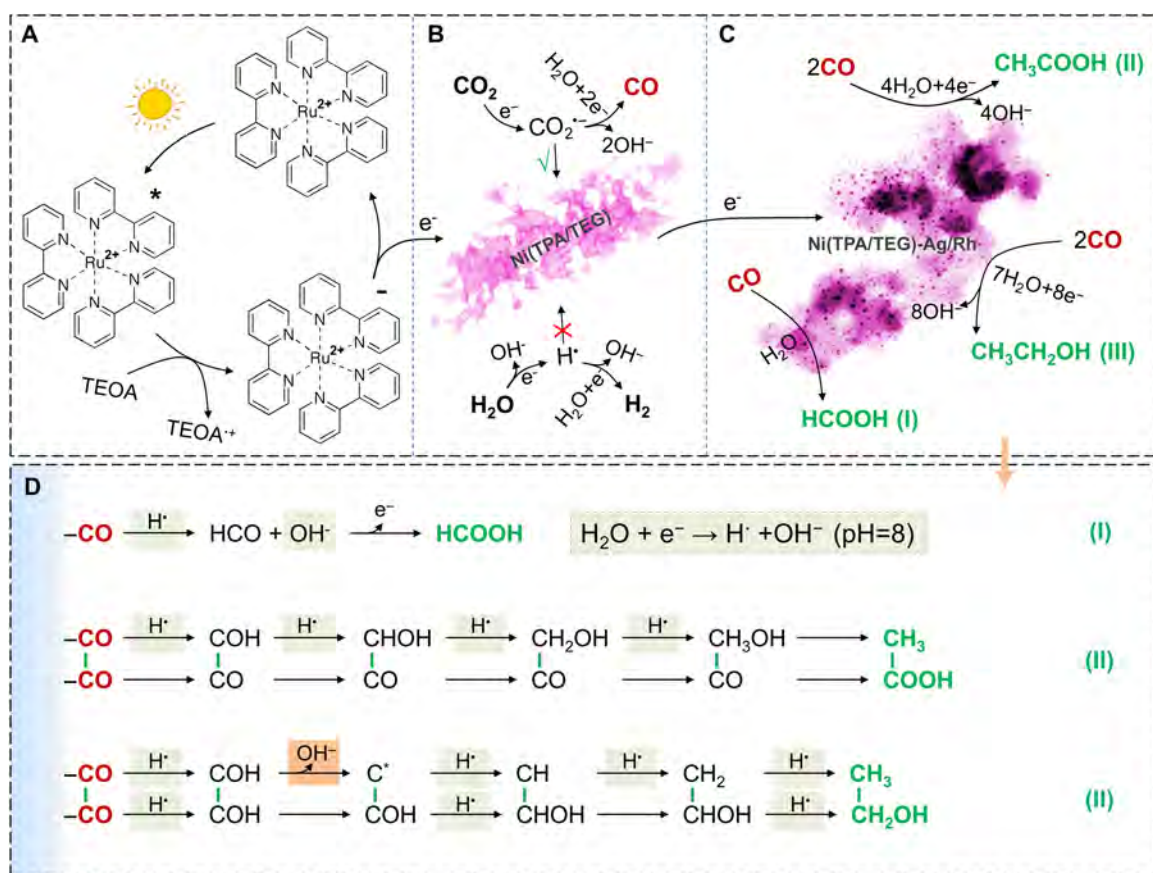


**Fig. 6. Proposed mechanisms for the photocatalytic conversion of  $\text{CO}_2$  to  $\text{CO}$  and of  $\text{CO}$  to other liquid products.** (A) Visible light reduction of the photosensitizer  $[\text{Ru}(\text{bpy})_3]^{2+}$ , which transfers an electron to the  $\text{Ni}(\text{TPA}/\text{TEG})$  catalyst to convert  $\text{CO}_2$  to  $\text{CO}$  (B) and to  $\text{Ni}(\text{TPA}/\text{TEG})-(\text{Ag}/\text{Rh})$  catalysts for the generation of  $\text{HCOOH}$ ,  $\text{CH}_3\text{COOH}$ , and  $\text{CH}_3\text{CH}_2\text{OH}$  from further reduction of  $\text{CO}$  (C). The STEM image in (C) is the Ag-decorated  $\text{Ni}(\text{TPA}/\text{TEG})$  catalyst (the original STEM image is shown in fig. S15). (D) Possible conversion pathways leading to the formation of  $\text{HCOOH}$ ,  $\text{CH}_3\text{COOH}$ , and  $\text{CH}_3\text{CH}_2\text{OH}$  via proton-coupled one-, four-, and eight-electron steps, respectively.

(262.19  $\mu\text{M}$ ),  $\text{HCOOH}$  (263.58  $\mu\text{M}$ ), and  $\text{CH}_3\text{COOH}$  (1178.04  $\mu\text{M}$ ). At pH 13, the hydroxyl ions ( $\text{OH}^-$ ) are commonly available for the hydroxylation of  $^*\text{CHO}$ , which favors the formation of  $\text{HCOOH}$  (fig. S18). On the contrary, the enhanced hydroxylation of  $^*\text{CHO}$  may suppress the kinetics of the multiprotonation of  $^*\text{CO}$  and the dehydroxylation of  $^*\text{CHO}$  (Fig. 6D), resulting in a lower amount of  $\text{CH}_3\text{COOH}$  and  $\text{CH}_3\text{CH}_2\text{OH}$  at pH 13. The appearance of  $\text{CH}_3\text{OH}$  may suggest a weak C-C coupling between  $^*\text{CH}_3\text{OH}$  and  $^*\text{CO}$  at pH 13 (leading to  $\text{CH}_3\text{COOH}$  at pH 8), which should be considered for the future  $\text{CO}_2/\text{CO}$  reduction catalyst design (49).

In summary, we have demonstrated a photochemical strategy for the design of novel nanostructured metal-organic materials, where the rigid TPA and soft TEG molecules are successfully cross-linked together with the  $\text{Ni}^{2+}$  centers. A spongy  $\text{Ni}(\text{TPA}/\text{TEG})$  hybrid structure with a considerably high concentration of defects has been achieved. We found that the  $\text{Ni}(\text{TPA}/\text{TEG})$  catalyst is remarkably active for  $\text{CO}$  production (with a production rate of 15,866  $\mu\text{mol hour}^{-1} \text{g}^{-1}$ ) from the heterogeneous photocatalytic  $\text{CO}_2$  reduction reaction, during which no other measurable competing gases such as  $\text{H}_2$  or  $\text{CH}_4$  are generated, thus giving a near 100%  $\text{CO}$  selectivity over other gases. When the spongy Ni-organic catalyst is enriched with Rh or Ag nanocrystals, formic acid and acetic acid can be produced selectively from the photocatalytic  $\text{CO}_2$  reduction reactions. We propose to use the spongy  $\text{Ni}(\text{TPA}/\text{TEG})$  catalyst in a “tandem catalyst” system to convert  $\text{CO}_2$  into high-value liq-

uid fuels using visible light, where the selectively  $\text{CO}_2$ -turned  $\text{CO}$  can be directly used as an intermediate gas reactant for the generation of liquid fuels, such as ethanol and acetic acid (fig. S19). More advanced metal-organic heterogeneous photocatalysts with improved  $\text{CO}_2$  fixation and light-harvesting capabilities are expected to be fabricated using the photochemical strategy for efficient solar-to-fuels conversion.

## MATERIALS AND METHODS

### Laser-chemical synthesis of metal-organic photocatalysts

All chemicals including nickel nitrate (99.99%), cobalt nitrate (99%), copper nitrate trihydrate (99%), ethanol (99.5%), DMF, TPA, and TEG were purchased from Sigma-Aldrich and used as received. The deionized water was produced by the Milli-Q Integral water purification system. A Continuum Surelite III nanosecond pulsed laser was used as a power source, and the following were the typical parameters of operation: wavelength, 1064 nm; frequency, 10 Hz; pulse width, 7 to 8 ns; beam diameter, 0.9 cm; and 700 mJ per pulse. TEG solutions (1 ml) of 1.5 M transition metal nitrates were added into 5 ml of DMF solution of 0.5 M TPA; the mixed solutions were stirred for 30 min before laser irradiation. For the syntheses of NiCo- and NiCoCu-organic frameworks, molar ratios of Ni/Co (1:1) and Ni/Co/Cu (1:1:1) were used, respectively. Typically, 3-hour laser irradiation was required for a 6-ml mixed precursor solution to complete the reaction. For the

syntheses by heating method, the same precursor solutions in glass vials were heated at 110°C in an oven for 48 hours. Precipitates produced after laser irradiations or heating were rinsed with acetone/ethanol, centrifuged at 9000 rpm for three times, and then dried in air at 60°C to obtain powders.

### Photocatalysis measurement of CO<sub>2</sub> reduction reactions

The visible light-driven photocatalytic CO<sub>2</sub> reduction was conducted in a closed gas circulation and evacuation system fitted with a top window Pyrex cell. A circulating cooling water system was used to maintain the reactor at around 20°C. In a typical reaction, 3 mg of catalyst (for each test), 2.5 mmol of Ru(bpy)<sub>3</sub>Cl<sub>2</sub>·6H<sub>2</sub>O, and 2 ml of TEOA were added to 10 ml of acetonitrile/H<sub>2</sub>O solvent mixture (CH<sub>3</sub>CN/H<sub>2</sub>O = 8:2). The pH value of the solution was ~8, which was tuned to 13 by 1 M NaOH aqueous solution for control experiment. The light source was a 300-W Xe lamp with a long-pass cutoff filter ( $\lambda > 420$  nm). Before light irradiation, the reaction system was evacuated and refilled with high-purity CO<sub>2</sub> (99.995%; SOXAL) several times to remove air inside and finally filled with CO<sub>2</sub> gas to reach a pressure of 400 torr. The evolved gas was detected by online GC (Agilent 7890A) equipped with a thermal conductivity detector and a flame ionization detector (FID) at different times of the photoreaction. To evaluate catalyst reusability, 15 mg of the catalyst was applied for photocatalysis and recycled by centrifugation after a 2-hour reaction, and then mixed with 8 ml of CH<sub>3</sub>CN, 2 ml of H<sub>2</sub>O, 2 ml of TEOA, and 18 mg of Ru(bpy)<sub>3</sub>Cl<sub>2</sub>·6H<sub>2</sub>O for the next run. The solution products in the liquid phase were analyzed separately at the end of the photoreaction. Alcohols in the liquid phase were analyzed by Agilent 7890A GC with an FID, a DB-WAX column, and helium as the carrier gas. Carboxylic acids in the liquid phase were analyzed using an Agilent 1260 high-performance liquid chromatograph (HPLC) with a PL Hi-Plex H column and variable wavelength detector (VWD) (210 nm). [Ru(bpy)<sub>3</sub>]Cl<sub>2</sub>·6H<sub>2</sub>O (99.95%) and TEOA ( $\geq 99.0\%$ ) were obtained from Sigma-Aldrich. The acetonitrile (HPLC-grade) was obtained from Merck.

The <sup>13</sup>CO<sub>2</sub> isotope tracer experiment was performed under similar photocatalytic reaction conditions. The reactor containing 3 mg of the catalyst, 2.5 mmol of Ru(bpy)<sub>3</sub>Cl<sub>2</sub>·6H<sub>2</sub>O, 2 ml of TEOA, and 10 ml of the CH<sub>3</sub>CN-H<sub>2</sub>O mixture solution (CH<sub>3</sub>CN/H<sub>2</sub>O = 8:2) was first evacuated to ensure air removal and then refilled with <sup>13</sup>CO<sub>2</sub> gas (99 atomic % <sup>13</sup>C; Aldrich) to reach a pressure of 400 torr. After 4 hours of irradiation, 200  $\mu$ l of gas products was withdrawn using a gas-tight syringe and then injected into a GC-MS (Agilent, GC Model 6890N/MS Model 5973) with a molecular sieve 5 Å column for analysis. The carboxylic acid analysis was carried out separately by using a Thermo Finnigan LCQ MS system.

### SUPPLEMENTARY MATERIALS

Supplementary material for this article is available at <http://advances.sciencemag.org/cgi/content/full/3/7/e1700921/DC1>

Materials characterizations

Three-dimensional tomographic reconstruction of the spongy Ni(TPA/TEG) network  
Comparison of the samples synthesized by laser-chemical route and traditional heating method  
Control experiments to confirm the origin of the evolved CO  
fig. S1. Structure of the selected rigid TPA linkers and soft TEG linkers for the laser synthesis of the nickel-organic photocatalyst.

fig. S2. Morphology and composition of the spongy Ni(TPA/TEG) composite.

fig. S3. Nitrogen physisorption measurements of the spongy Ni(TPA/TEG) catalyst.

fig. S4. A comparison between the measured and simulated powder XRD patterns of the crystalline Ni(TPA) framework.

fig. S5. Electron diffraction of the Ni(TPA/TEG) catalyst.

fig. S6. STEM images show the morphologies of five nickel-organic composites synthesized either by the laser-chemical approach (L) or the conventional heating method (H).

fig. S7. Comparison of the structure of Ni(TPA/TEG) and Ni(TPA) composites synthesized by both laser-chemical (L) and heating (H) methods.

fig. S8. Brunauer-Emmett-Teller surface area of five as-synthesized nickel-organic composites, including Ni(TPA/TEG) (L), Ni(TEG) (L), Ni(TPA)-DMF (L), Ni(TPA)-TEG (H), and Ni(TPA)-DMF (H).

fig. S9. CO production rate on different amounts of the Ni(TPA/TEG) catalyst.

fig. S10. Powder XRD patterns of the spongy Ni(TPA/TEG) catalyst before and after 24-hour photocatalytic reactions.

fig. S11. Controlled photocatalysis experiments by applying the Ni(TPA/TEG) (L) catalyst in either CO<sub>2</sub> or He gas, and without adding catalyst in CO<sub>2</sub>.

fig. S12. Comparison of the morphology and structure of the five laser-synthesized M(TPA/TEG) (M = Ni, Co, Cu) catalysts, including Ni(TPA/TEG), NiCo(TPA/TEG), Co(TPA/TEG), NiCoCu(TPA/TEG), and Cu(TPA/TEG).

fig. S13. Comparison of the yield of CO and H<sub>2</sub> on five laser-synthesized M(TPA/TEG) (M = Ni, Co, Cu) catalysts after a 6-hour photocatalytic CO<sub>2</sub> reduction reaction.

fig. S14. Comparison of the gas products evolved from the laser-synthesized Ni(TPA/TEG) and Ni(TEG) catalysts.

fig. S15. MS of acetic acid (CH<sub>3</sub>COOH) produced from the photocatalytic reduction of CO<sub>2</sub> using the Ni(TPA/TEG)-Ag catalyst.

fig. S16. Comparison of the liquid products generated from photocatalytic CO<sub>2</sub>RR and CORR on the Ni(TPA/TEG)-Rh catalyst.

fig. S17. STEM image of the Ag-decorated Ni(TPA/TEG) catalyst.

fig. S18. Comparison of the liquid products generated from photocatalytic CO reduction reactions on the Ni(TPA/TEG)-Ag catalyst at pH 8 and 13.

fig. S19. Proposed three-cell tandem photocatalytic CO<sub>2</sub> reduction system for liquid fuels production.

table S1. List of other heterogeneous catalysts used for photocatalytic CO<sub>2</sub>-to-CO conversion.  
movie S1. Three-dimensional reconstructed tomography of a fraction of the spongy Ni(TPA/TEG) composite.

movie S2. Scanning nanobeam diffraction pattern series showing the [100] orientation of the spongy Ni(TPA/TEG) composite.

movie S3. Scanning nanobeam diffraction pattern series taken along the [111] orientation of the spongy Ni(TPA/TEG) composite.

References (50–55)

### REFERENCES AND NOTES

1. A. Cho, Energy's tricky tradeoffs. *Science* **329**, 786–787 (2010).
2. S. J. Davis, K. Caldeira, H. D. Matthews, Future CO<sub>2</sub> emissions and climate change from existing energy infrastructure. *Science* **329**, 1330–1333 (2010).
3. N. S. Lewis, D. G. Nocera, Powering the planet: Chemical challenges in solar energy utilization. *Proc. Natl. Acad. Sci. U.S.A.* **103**, 15729–15735 (2006).
4. S. R. Loarie, P. B. Duffy, H. Hamilton, G. P. Asner, C. B. Field, D. D. Ackerly, The velocity of climate change. *Nature* **462**, 1052–1055 (2009).
5. M. R. Allen, D. J. Frame, C. Huntingford, C. D. Jones, J. A. Lowe, M. Meinshausen, N. Meinshausen, Warming caused by cumulative carbon emissions towards the trillionth tonne. *Nature* **458**, 1163–1166 (2009).
6. K. B. Tokarska, N. P. Gillett, A. J. Weaver, V. K. Arora, M. Eby, The climate response to five trillion tonnes of carbon. *Nat. Clim. Change* **6**, 851–855 (2016).
7. R. A. Feely, C. L. Sabine, K. Lee, W. Berelson, J. Kleypas, V. J. Fabry, F. J. Millero, Impact of anthropogenic CO<sub>2</sub> on the CaCO<sub>3</sub> system in the oceans. *Science* **305**, 362–366 (2004).
8. T. Wheeler, J. von Braun, Climate change impacts on global food security. *Science* **341**, 508–513 (2013).
9. M. C. Urban, Accelerating extinction risk from climate change. *Science* **348**, 571–573 (2015).
10. J. S. Pal, E. A. B. Eltahir, Future temperature in southwest Asia projected to exceed a threshold for human adaptability. *Nat. Clim. Change* **6**, 197–200 (2016).
11. R. James, F. Otto, H. Parker, E. Boyd, R. Cornforth, D. Mitchell, M. Allen, Characterizing loss and damage from climate change. *Nat. Clim. Change* **4**, 938–939 (2014).
12. D. W. Keith, Why capture CO<sub>2</sub> from the atmosphere? *Science* **325**, 1654–1655 (2009).
13. N. S. Lewis, Research opportunities to advance solar energy utilization. *Science* **351**, aad1920 (2016).
14. M. Mikkelsen, M. Jorgensen, F. C. Krebs, The teraton challenge. A review of fixation and transformation of carbon dioxide. *Energy Environ. Sci.* **3**, 43–81 (2010).
15. J. L. White, M. F. Baruch, J. E. Pander III, Y. Hu, I. C. Fortmeyer, J. E. Park, T. Zhang, K. Liao, J. Gu, Y. Yan, T. W. Shaw, E. Abelev, A. B. Bocarsly, Light-driven heterogeneous reduction of carbon dioxide: Photocatalysts and photoelectrodes. *Chem. Rev.* **115**, 12888–12935 (2015).
16. K. Iizuka, T. Wato, Y. Miseki, K. Saito, A. Kudo, Photocatalytic reduction of carbon dioxide over Ag cocatalyst-loaded Al<sub>0.4</sub>Ti<sub>4</sub>O<sub>15</sub> (A = Ca, Sr, and Ba) using water as a reducing reagent. *J. Am. Chem. Soc.* **133**, 20863–20868 (2011).

17. S. N. Habisreutingir, L. Schmidt-Mende, J. K. Stolarczyk, Photocatalytic reduction of CO<sub>2</sub> on TiO<sub>2</sub> and other semiconductors. *Angew. Chem. Int. Ed.* **52**, 7372–7408 (2013).
18. C. Gao, Q. Meng, K. Zhao, H. Yin, D. Wang, J. Guo, S. Zhao, L. Chang, M. He, Q. Li, H. Zhao, X. Huang, Y. Gao, Z. Tang, Co<sub>3</sub>O<sub>4</sub> hexagonal platelets with controllable facets enabling highly efficient visible-light photocatalytic reduction of CO<sub>2</sub>. *Adv. Mater.* **28**, 6485–6490 (2016).
19. S. Wang, W. Yao, J. Lin, Z. Ding, X. Wang, Cobalt imidazolate metal–organic frameworks photosplit CO<sub>2</sub> under mild reaction conditions. *Angew. Chem. Int. Ed.* **53**, 1034–1038 (2014).
20. A. Louidice, P. Lobaccaro, E. A. Kamali, T. Thao, B. H. Huang, J. W. Ager, R. Buonsanti, Tailoring copper nanocrystals towards C<sub>2</sub> products in electrochemical CO<sub>2</sub> reduction. *Angew. Chem. Int. Ed.* **55**, 5789–5792 (2016).
21. K. P. Kuhl, E. R. Cave, D. N. Abram, T. F. Jaramillo, New insights into the electrochemical reduction of carbon dioxide on metallic copper surfaces. *Energy Environ. Sci.* **5**, 7050–7059 (2012).
22. M. R. Singh, E. L. Clark, A. T. Bell, Thermodynamic and achievable efficiencies for solar-driven electrochemical reduction of carbon dioxide to transportation fuels. *Proc. Natl. Acad. Sci. U.S.A.* **112**, E6111–E6118 (2015).
23. K.-Y. Niu, F. Lin, S. Jung, L. Fang, D. Nordlund, C. C. L. McCrory, T.-C. Weng, P. Ercius, M. M. Doeff, H. Zheng, Tuning complex transition metal hydroxide nanostructures as active catalysts for water oxidation by a laser–chemical route. *Nano Lett.* **15**, 2498–2503 (2015).
24. J. Kothandaraman, A. Goeppert, M. Czaun, G. A. Olah, G. K. S. Prakash, Conversion of CO<sub>2</sub> from air into methanol using a polyamine and a homogeneous ruthenium catalyst. *J. Am. Chem. Soc.* **138**, 778–781 (2016).
25. H. Furukawa, K. E. Cordova, M. O’Keeffe, O. M. Yaghi, The chemistry and applications of metal–organic frameworks. *Science* **341**, 1230444 (2013).
26. K. Sumida, D. L. Rogow, J. A. Mason, T. M. McDonald, E. D. Bloch, Z. R. Herm, T.-H. Bae, J. R. Long, Carbon dioxide capture in metal–organic frameworks. *Chem. Rev.* **112**, 724–781 (2012).
27. W. Lu, Z. Wei, Z.-Y. Gu, T.-F. Liu, J. Park, J. Park, J. Tian, M. Zhang, Q. Zhang, T. Gentle III, M. Bosch, H.-C. Zhou, Tuning the structure and function of metal–organic frameworks via linker design. *Chem. Soc. Rev.* **43**, 5561–5593 (2014).
28. C. G. Carson, K. Hardcastle, J. Schwartz, X. Liu, C. Hoffmann, R. A. Gerhardt, R. Tannenbaum, Synthesis and structure characterization of copper terephthalate metal–organic frameworks. *Eur. J. Inorg. Chem.* **2009**, 2338–2343 (2009).
29. Y. Tomita, S. Teruya, O. Koga, Y. Hori, Electrochemical reduction of carbon dioxide at a platinum electrode in acetonitrile–water mixtures. *J. Electrochem. Soc.* **147**, 4164–4167 (2000).
30. M. Kirch, J.-M. Lehn, J.-P. Sauvage, Hydrogen generation by visible light irradiation of aqueous solutions of metal complexes. An approach to the photochemical conversion and storage of solar energy. *Helv. Chim. Acta* **62**, 1345–1384 (1979).
31. T. W. Woolerton, S. Sheard, E. Pierce, S. W. Ragsdale, F. A. Armstrong, CO<sub>2</sub> photoreduction at enzyme-modified metal oxide nanoparticles. *Energy Environ. Sci.* **4**, 2393–2399 (2011).
32. H. Takeda, K. Ohashi, A. Sekine, O. Ishitani, Photocatalytic CO<sub>2</sub> reduction using Cu(I) photosensitizers with a Fe(II) catalyst. *J. Am. Chem. Soc.* **138**, 4354–4357 (2016).
33. S. Sato, T. Morikawa, S. Saeki, T. Kajino, T. Motohiro, Visible-light-induced selective CO<sub>2</sub> reduction utilizing a ruthenium complex electrocatalyst linked to a p-Type nitrogen-doped Ta<sub>2</sub>O<sub>5</sub> semiconductor. *Angew. Chem. Int. Ed.* **49**, 5101–5105 (2010).
34. R. Kuriki, H. Matsunaga, T. Nakashima, K. Wada, A. Yamakata, O. Ishitani, K. Maeda, Nature-inspired, highly durable CO<sub>2</sub> reduction system consisting of a binuclear ruthenium(II) complex and an organic semiconductor using visible light. *J. Am. Chem. Soc.* **138**, 5159–5170 (2016).
35. U. Maitra, B. S. Naidu, A. Govindaraj, C. N. R. Rao, Importance of trivalency and the e<sub>g</sub><sup>1</sup> configuration in the photocatalytic oxidation of water by Mn and Co oxides. *Proc. Natl. Acad. Sci. U.S.A.* **110**, 11704–11707 (2013).
36. J. Luo, J.-H. Im, M. T. Mayer, M. Schreiber, M. K. Nazeeruddin, N.-G. Park, S. D. Tilley, H. J. Fan, M. Grätzel, Water photolysis at 12.3% efficiency via perovskite photovoltaics and earth-abundant catalysts. *Science* **345**, 1593–1596 (2014).
37. M. W. Kanan, D. G. Nocera, In situ formation of an oxygen-evolving catalyst in neutral water containing phosphate and Co<sup>2+</sup>. *Science* **321**, 1072–1075 (2008).
38. X. Xie, Y. Li, Z.-Q. Liu, M. Haruta, W. Shen, Low-temperature oxidation of CO catalysed by Co<sub>3</sub>O<sub>4</sub> nanorods. *Nature* **458**, 746–749 (2009).
39. S. Lin, C. S. Diercks, Y.-B. Zhang, N. Kornienko, E. M. Nichols, Y. Zhao, A. R. Paris, D. Kim, P. Yang, O. M. Yaghi, C. J. Chang, Covalent organic frameworks comprising cobalt porphyrins for catalytic CO<sub>2</sub> reduction in water. *Science* **349**, 1208–1213 (2015).
40. C. W. Li, M. W. Kanan, CO<sub>2</sub> reduction at low overpotential on Cu electrodes resulting from the reduction of thick Cu<sub>2</sub>O films. *J. Am. Chem. Soc.* **134**, 7231–7234 (2012).
41. R. Kortlever, I. Peters, S. Koper, M. T. M. Koper, Electrochemical CO<sub>2</sub> reduction to formic acid at low overpotential and with high faradaic efficiency on carbon-supported bimetallic Pd–Pt nanoparticles. *ACS Catal.* **5**, 3916–3923 (2015).
42. K. P. Kuhl, T. Hatsukade, E. R. Cave, D. N. Abram, J. Kibsgaard, T. F. Jaramillo, Electrochemical conversion of carbon dioxide to methane and methanol on transition metal surfaces. *J. Am. Chem. Soc.* **136**, 14107–14113 (2014).
43. F. Gärtner, B. Sundararaju, A.-E. Surkus, A. Boddien, B. Loges, H. Junge, P. H. Dixneuf, M. Beller, Light-driven hydrogen generation: Efficient iron-based water reduction catalysts. *Angew. Chem. Int. Ed.* **48**, 9962–9965 (2009).
44. T. Maschmeyer, M. Che, Catalytic aspects of light-induced hydrogen generation in water with TiO<sub>2</sub> and other photocatalysts: A simple and practical way towards a normalization? *Angew. Chem. Int. Ed.* **49**, 1536–1539 (2010).
45. J. Shen, R. Kortlever, R. Kas, Y. Y. Birdja, O. Diaz-Morales, Y. Kwon, I. Ledezma-Yanez, K. J. P. Schouten, G. Mul, M. T. M. Koper, Electrocatalytic reduction of carbon dioxide to carbon monoxide and methane at an immobilized cobalt protoporphyrin. *Nat. Commun.* **6**, 8177 (2015).
46. A. Wuttig, M. Yaguchi, K. Motobayashi, M. Osawa, Y. Surendranath, Inhibited proton transfer enhances Au-catalyzed CO<sub>2</sub>-to-fuels selectivity. *Proc. Natl. Acad. Sci. U.S.A.* **113**, E4585–E4593 (2016).
47. T. Cheng, H. Xiao, W. A. Goddard III, Full atomistic reaction mechanism with kinetics for CO reduction on Cu(100) from ab initio molecular dynamics free-energy calculations at 298 K. *Proc. Natl. Acad. Sci. U.S.A.* **114**, 1795–1800 (2017).
48. C. W. Li, J. Ciston, M. W. Kanan, Electroreduction of carbon monoxide to liquid fuel on oxide-derived nanocrystalline copper. *Nature* **508**, 504–507 (2014).
49. R. E. London, T. E. Walker, V. H. Kollman, N. A. Matwijoff, Studies of the pH dependence of <sup>13</sup>C shifts and carbon-carbon coupling constants of [U-13]aspartic and α-glutamic acids. *J. Am. Chem. Soc.* **100**, 3723–3729 (1978).
50. H. Jiang, Y. Cheng, L. Yuan, A Langmuir-like desorption model for reflecting the inhomogeneous pore structure of coal and its experimental verification. *RSC Adv.* **5**, 2434–2440 (2015).
51. S. Wang, X. Wang, Photocatalytic CO<sub>2</sub> reduction by CdS promoted with a zeolitic imidazolate framework. *Appl. Catal. B* **162**, 494–500 (2015).
52. S. Wang, Z. Ding, X. Wang, A stable ZnCo<sub>2</sub>O<sub>4</sub> cocatalyst for photocatalytic CO<sub>2</sub> reduction. *Chem. Commun.* **51**, 1517–1519 (2015).
53. S. Wang, Y. Hou, X. Wang, Development of a stable MnCo<sub>2</sub>O<sub>4</sub> cocatalyst for photocatalytic CO<sub>2</sub> reduction with visible light. *ACS Appl. Mater. Interfaces* **7**, 4327–4335 (2015).
54. R. Kuriki, K. Sekizawa, O. Ishitani, K. Maeda, Visible-light-driven CO<sub>2</sub> reduction with carbon nitride: Enhancing the activity of ruthenium catalysts. *Angew. Chem. Int. Ed.* **54**, 2406–2409 (2015).
55. H. Takeda, H. Koizumi, K. Okamoto, O. Ishitani, Photocatalytic CO<sub>2</sub> reduction using a Mn complex as a catalyst. *Chem. Commun.* **50**, 1491–1493 (2014).

**Acknowledgments:** We acknowledge C. Gammner for developing the Foundry users’ code for electron scanning diffraction experiments and analysis and Y. Liu at Lawrence Berkeley National Laboratory (LBNL) for help with FTIR spectroscopy measurements. **Funding:** We used TEM facilities in the Molecular Foundry at LBNL, which was supported by the U.S. Department of Energy (DOE), Office of Science, Office of Basic Energy Sciences, under contract #DE-AC02-05CH11231. Electron tomography studies used resources of the Center for Functional Nanomaterials, which is a DOE Office of Science facility, at Brookhaven National Laboratory under contract no. DE-SC0012704. This work was also supported by the Assistant Secretary for Energy Efficiency and Renewable Energy, Office of Vehicle Technologies of the DOE, under contract no. DE-AC02-05CH11231. All materials synthesis was carried out at LBNL and was supported by the DOE, Office of Science, Office of Basic Energy Sciences Materials Sciences and Engineering Division, under contract no. DE-AC02-05-CH11231 within the Early Career program MSE08 (to H.Z.). Y.X. and R.X. acknowledge financial support from Nanyang Technological University. K.N. and Y.L. were partially supported by the SinBeRise program of BEARS (Berkeley Education Alliance for Research in Singapore) at University of California, Berkeley. **Author contributions:** K.N. designed and performed the experiments, analyzed the experimental data, and wrote the manuscript. Y.X. and R.X. performed the photocatalysis experiments. H.W. performed the laser-chemical synthesis. H.L.X. performed the three-dimensional tomographic reconstruction. R.Y., F.L., C.T., Y.L., and K.C.B. helped on materials structure analyses. M.M.D., J.A., and M.T.M.K. contributed to the manuscript writing and catalytic mechanism discussions. All work was carried out under the supervision of H.Z. **Competing interests:** The authors declare that they have no competing interests. **Data and materials availability:** All data needed to evaluate the conclusions in the paper are present in the paper and/or the Supplementary Materials. Additional data related to this paper may be requested from the authors.

Submitted 24 March 2017

Accepted 27 June 2017

Published 28 July 2017

10.1126/sciadv.1700921

**Citation:** K. Niu, Y. Xu, H. Wang, R. Ye, H. L. Xin, F. Lin, C. Tian, Y. Lum, K. C. Bustillo, M. M. Doeff, M. T. M. Koper, J. Ager, R. Xu, H. Zheng, A spongy nickel-organic CO<sub>2</sub> reduction photocatalyst for nearly 100% selective CO production. *Sci. Adv.* **3**, e1700921 (2017).

## A spongy nickel-organic CO<sub>2</sub> reduction photocatalyst for nearly 100% selective CO production

Kaiyang Niu, You Xu, Haicheng Wang, Rong Ye, Huolin L. Xin, Feng Lin, Chixia Tian, Yanwei Lum, Karen C. Bustillo, Marca M. Doeff, Marc T. M. Koper, Joel Ager, Rong Xu and Haimei Zheng

*Sci Adv* **3** (7), e1700921.  
DOI: 10.1126/sciadv.1700921

### ARTICLE TOOLS

<http://advances.sciencemag.org/content/3/7/e1700921>

### SUPPLEMENTARY MATERIALS

<http://advances.sciencemag.org/content/suppl/2017/07/24/3.7.e1700921.DC1>

### PERMISSIONS

<http://www.sciencemag.org/help/reprints-and-permissions>

Use of this article is subject to the [Terms of Service](#)

---

*Science Advances* (ISSN 2375-2548) is published by the American Association for the Advancement of Science, 1200 New York Avenue NW, Washington, DC 20005. The title *Science Advances* is a registered trademark of AAAS.

Copyright © 2017 The Authors, some rights reserved; exclusive licensee American Association for the Advancement of Science. No claim to original U.S. Government Works. Distributed under a Creative Commons Attribution NonCommercial License 4.0 (CC BY-NC).